Journal of Low Temperature Physics
https://doi.org/10.1007/s10909-024-03204-z

Advances in the Goertzel Filter Bank Channelizer for Cryogenic Sensors Readout

L. P. Ferreyro[1,2,4] · M. E. García Redondo[1,2,4] · J. M. Salum[1,2] · T. Muscheid[2] · M. Hampel[1,4] · A. Almela[1,4] · A. Fuster[1,4] · J. M. Geria[1,3,4] · J. Bonaparte[2,4] · J. Bonilla-Neira[1,3] · L. E. Ardila-Perez[2] · R. Gartmann[2] · N. Müller[1,3] · M. Wegner[3] · O. Sander[2] · M. Platino[1] · S. Kempf[2,3] · A. Etchegoyen[1] · M. Weber[2]

Received: 3 November 2023 / Accepted: 17 August 2024

Abstract
Neutrino mass estimation experiments and cosmic microwave background (CMB) radiation surveys both employ low-temperature detectors (LTD) known as calorimeters and bolometers, respectively. These detectors operate typically between 10 and 300 mK. LTDs multiplexed by means of a microwave superconducting quantum interference device multiplexer (μMUX) demonstrated to be an excellent device for the readout of several detectors in the microwave region. This entails generating a multi-tonal signal and its subsequent readout. A single-tone detection method based on a Goertzel filter bank (GFB) channelizer was used for the readout of the aforementioned signal, implemented in a software-defined radio readout architecture within a field-programmable gate array. The measurements presented here demonstrate remarkable results in validating the suitability of the GFB channelizer for this system.

Keywords Goertzel · FPGA · Magnetic microbolometer · Magnetic microcalorimeter

✉ L. P. Ferreyro
luciano.ferreyro@iteda.cnea.gov.ar

[1] ITeDA (CNEA-CONICET-UNSAM), Buenos Aires, Argentina

[2] Institute for Data Processing and Electronics (IPE), Karlsruhe Institute of Technology (KIT), Karlsruhe, Germany

[3] Institute of Micro- and Nanoelectronic Systems (IMS), Karlsruhe Institute of Technology (KIT), Karlsruhe, Germany

[4] Universidad Tecnológica Nacional (UTN), Buenos Aires, Argentina

Published online: 12 September 2024

1 Introduction

The electron capture in ^{163}Ho (ECHo) [1] experiment aims to investigate the neutrino mass in the sub-eV region, analyzing the end-point region of the ^{163}Ho electron capture spectrum. Large arrays of magnetic microcalorimeters (MMCs) [2], implanted with ^{163}Ho, operated in parallel are planned to be used for this purpose to ultimately acquire a statistically significant volume of data.

The Q &U Bolometric Interferometer for Cosmology (QUBIC) [3] will contribute in the quest of finding the so-called *smoking gun* of inflation [4, 5], by detecting and characterizing the B-modes polarization of the cosmic microwave background (CMB) radiation (primordial tensorial perturbations in the metric). QUBIC relies on transition edge sensor (TES) bolometers [6] as of now; however, a new bolometer has recently been proposed to the collaboration. The bolometer, a magnetic microbolometer (MMB), is based on the developed paramagnetic sensor of the MMC [7].

Cryogenic sensing, such as the introduced neutrino mass estimation experiments and CMB surveys present challenges to be addressed, not only in the low-temperature detectors but also in the warm electronics, driving continuous improvements in both cases. These include achieving higher sensitivity, reducing dissipation at mK stages, and increasing multiplexing factors, among others. The pursuit of a higher multiplexing factor naturally leads to microwave superconducting quantum interference device (SQUID) multiplexing (μMUX) [8], which involves the injection and subsequent readout of a multi-tonal signal.

Single-tone detection methods, used for detecting each individual frequency component of the aforementioned multi-tonal signal, turn out to be an attractive approach as they mainly improve the configuration flexibility for run-time re-configuration, and the control of the spectral leakage in this kind of systems.

The Goertzel filter enables the calculation of a single bin of a signal's discrete Fourier transform (DFT), the kth bin of an N-point DFT, defined by:

$$X[k] = \sum_{n=0}^{N-1} x[n] e^{-j2\pi k \frac{n-N}{N}} \tag{1}$$

It can be represented by a second-order infinite impulse response (IIR) filter with its z-domain transfer function [9]:

$$H_k(z) = \frac{1 - e^{-j\frac{2\pi k}{N}} z^{-1}}{1 - 2\cos(\frac{2\pi k}{N}) z^{-1} + z^{-2}} \tag{2}$$

We present in this article an update on the suitability analysis of the Goertzel filter bank (GFB) channelizer, sketched in Fig. 1. Here we show measurements of a μMUX channel regarding demodulation capabilities and noise level in a cryogenic setup, extending the results presented in [9].

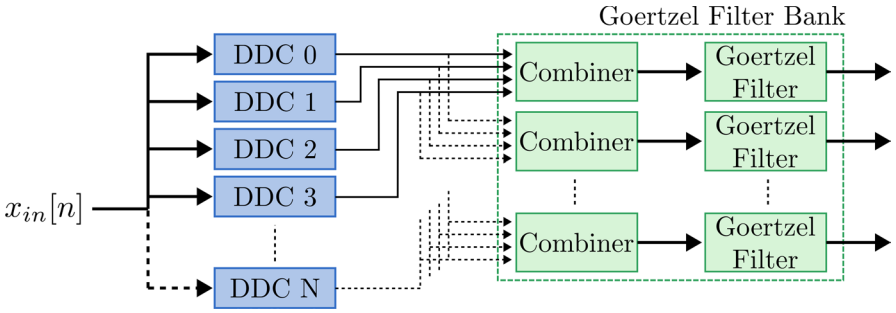

Fig. 1 Goertzel Filter Bank Channelizer: It consists of a preceding decimation stage carried out by digital down converters (DDCs) (other techniques, such as polyphase filter banks, can also be used in this part), allowing a coarse tuning for processing the bands of interest where the different μMUX resonances might be; and then the GFB is used for fine tuning and individual tone detection. In our current implementation, each Goertzel filter can detect four independent frequency components, and the logic circuits run at 250 MHz

2 Readout System

Reading sensors multiplexed by means of a μMUX requires the generation of multi-tonal signals in the microwave range. A software-defined radio (SDR) system (sketched in Fig. 2) is required for carrying out this intricate task. The basic elements of the SDR system are a so-called radio-frequency (RF) front-end, which performs the tasks of signal up-conversion and down-conversion, spectrum splitting, and merging; also, the digital-to-analog and analog-to-digital converters (DAC and ADC, respectively), which basically connect the digital world with the analog world; and the digital electronics, where the intensive data processing occurs. The AMD ZCU102 [10] evaluation board is used for the digital backend block, equipped with the Zynq UltraScale+ MPSoC. The AD-FMCDAQ2-EBZ [11] board houses a DAC (AD9144) and an ADC (AD9680). The RF

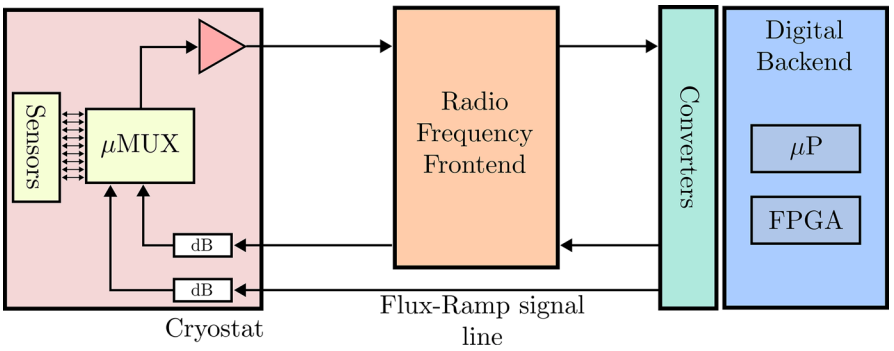

Fig. 2 The readout system including the cryogenic setup. The cryostat consists of different temperature stages, not shown in this diagram. The low-noise amplifier (LNA), represented by the red triangle, operates on the 4 K stage. The μMUX and the sensors are located in the lowest temperature stage, for example, 320 mK for QUBIC and 20 mK for ECHo

front-end is a custom two-stage heterodyne mixer stage board which later resulted in a scaled-up revision for the ECHo readout electronics [12].

3 Experimental Setup

The cryogenic setup consists of a Bluefors LD250 dilution refrigerator [13] and two signal paths: a transmission one and a reception one. The former introduces a total attenuation of 40 dB due to two cryo-attenuators (10 dB at the 50 K and 10 dB at the 4 K stage) and a 20 dB directional coupler in the 10 mK stage. A CMB-optimized 9-channel μMUX is connected to the directional coupler in that cooling stage. The latter contains a circulator (connected to the μMUX), 0 dB attenuators (for thermalization reasons), and a 35 dB gain LNA [14] at the 4 K stage [15].

The μMUX was placed without attached sensors in the mixing chamber (MXC), which has a base temperature of 10 mK and was set to work at 100 mK. Its frequency response is shown in Fig. 3. For the flux-ramp modulation (FRM), a Picotest G5100A [16] was used. The carrier readout power was of – 40 dBm at the cryostat input, yielding approx. – 80 dBm at the chip.

The channel located at approx. 3.9656 GHz was used for the demodulation capabilities tests. This SQUID resonator in the μMUX has a period of 189.76 μA per flux-quantum Φ_0 and a bandwidth of roughly 200 kHz. The mutual inductance between the SQUIDs and the resonators is of 3.5 pH, and between the SQUIDs and the modulation coils is of 10 pH.

4 Measurements Results

The amplitude power spectral density (PSD) at the output of the GFB channelizer for a window size of 32 samples and a flat-top window function is shown in Fig. 4. To quantify noise floor variation, a direct loopback in the back-end was applied with

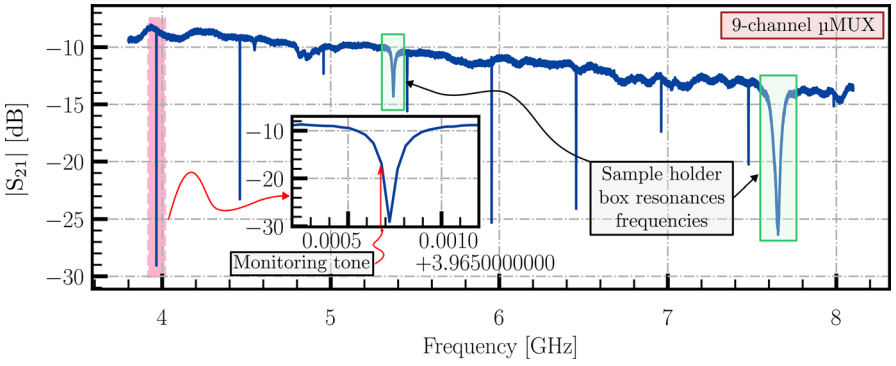

Fig. 3 9-channel μMUX measurements using a Keysight PNA-X N5242B. The highlighted channel (in red), at 3.9656 GHz, is the one used for measurements in this work

and without the RF front-end. Two different carrier signals at – 145.8 MHz were generated at the DAC output: – 1 dBm and – 40 dBm. The RF front-end introduces an attenuation of 15 dB in the transmission path, regardless of the input power, and provides around 7 dB of gain in the receiver path (after demodulation, applied separately to the I and Q components). This results in a net attenuation of roughly 5 dB for the complex envelope signal (which has 3 dB more power than the individual I and Q components) in the RF loopback, as illustrated in Fig. 4. For the selected channel readout and monitoring tone location (for amplitude domain demodulation, see Fig. 3, zoom), the RF front-end local oscillator was placed at 4.111 GHz.

Also, the spurious components have different sources, like the rf-SQUID's termination in the μMUX (no input coil attached), ADC, and the electromagnetic interference coming from the surrounding area.

To characterize the demodulation capabilities of the channelizer, we proceed as described in [9] but with a cryogenic device at 100 mK. Different flux-ramp sawtooth signals varying in frequency (f_{ramp}) and amplitude (for different number of flux-quanta) were generated for modulation of the SQUID. The different combinations of f_{ramp} and ramp amplitude yield different SQUID frequencies, f_{mod}. The readout power at the DAC output was again −40 dBm.

Figure 5 (top) shows the GFB output for a sawtooth signal with $f_{ramp} = 1$ kHz. Three different maximum amplitude values were used, matching one, two, and

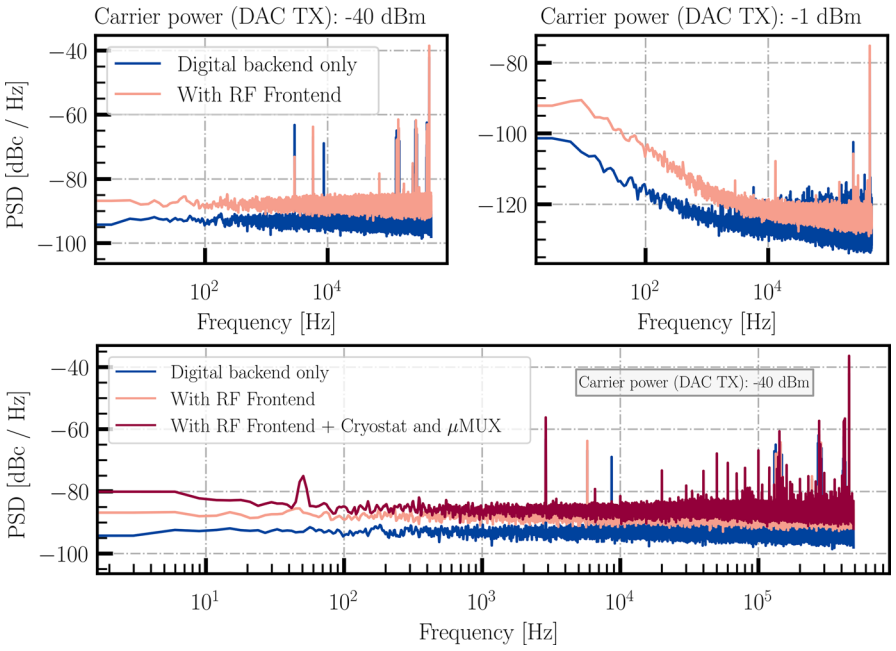

Fig. 4 Noise performance. A 32 sample window size was utilized in this case, with two different power levels generated with the DACs, – 1 dBm and – 40 dBm at the DAC output. The real input power value (at the ADC) is 5 dB less (∼ – 45 dBm and ∼ – 6 dBm) (top). Same but including the cryogenic setup (bottom)

four Φ_0; delivering consistent f_{mod} of 1 kHz, 2 kHz, and 4 kHz, respectively. The mean value of the GFB was removed (the carrier input power) for visualization purposes and clarity of the result.

These results show the impact of the f_{ramp}. The sawtooth phase jumps in the time domain, understood as a Dirac delta pulse $\delta(t)$, give rise to harmonic contributions in the spectrum equally spaced every f_{ramp} (a frequency comb), being 1 kHz for this test. Meanwhile, the stronger components belong to the f_{mod}: 1 kHz, 2 kHz, and 4 kHz.

As no detector was available for this test, a sinusoidal emulation signal $d(t)$, at different frequencies and modulation indices, was added. This approach was implemented by using $y(t) = A \cdot \text{ramp}[2\pi f_{ramp} t + d(t)]$, $y(t)$ as signal generator output. This emulates a phase modulation (PM) scenario. For visualization purposes, only the case of 135 Hz and a modulation index of 10 ° (phase deviation peak value) are

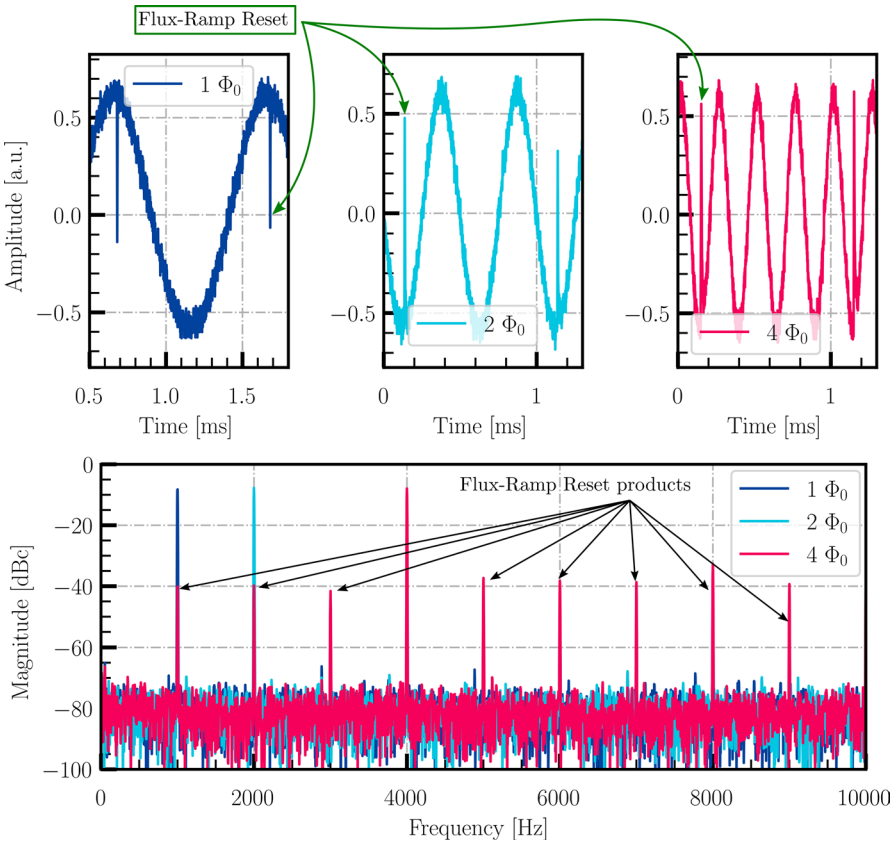

Fig. 5 GFB output. A sawtooth of f_{ramp} = 1 kHz was generated with different amplitudes for one, two, and four quantum-fluxes (Φ_0). The expected result is that f_{mod} is N_{Φ_0} times the sawtooth frequency. The sawtooth reset is visible in the images (top). The frequency spectrum of the channelized signals with the sawtooth reset products, marked in the plot (bottom)

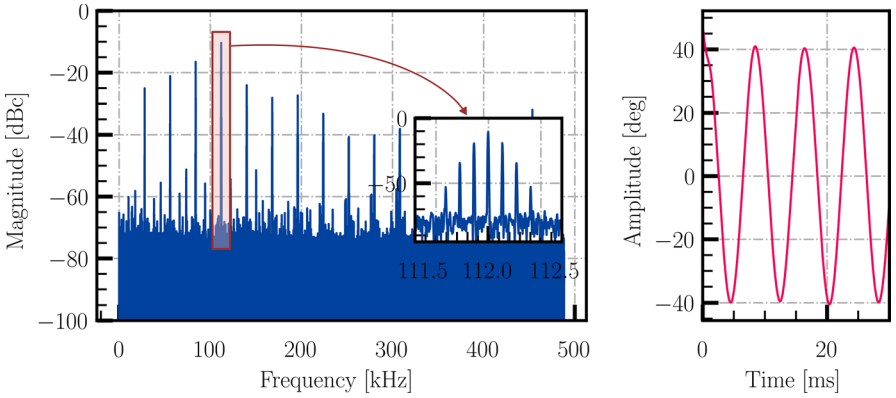

Fig. 6 FFT of one of the acquisitions with detector emulation: $f_{ramp} = 28$ kHz and $f_{det} = 135$ Hz, with an amplitude of four Φ_0. The highlighted FFT bin represents the SQUID frequency, with the PM sidelobes visible around it (left). Quadrature demodulation of the detector signal (phase deviation) for four Φ_0. The result is consistent with the expected value of four times the detector signal. (right)

shown in Fig. 6. The demodulated [17, 18] signal from the GFB output is depicted in Fig. 6, right.

The GFB output is not shown in its time domain form as it is visually the same as the already presented plots like Fig. 5 (top), but instead, their FFT is presented in Fig. 6 (left). An f_{ramp} of 28 kHz with an amplitude of four Φ_0 was generated, yielding an f_{mod} of 112 kHz, visible in the zoom image of Fig. 6. There, the highlighted FFT bin represents the SQUID frequency, f_{mod}, together with the components of the generated PM of 135 Hz. The output of the quadrature demodulation was passed through a digital Butterworth low-pass filter of fourth order and a f_{cut} at 500 Hz, in order to remove the high-frequency components

5 Conclusion

It was verified that this method is capable of demodulating a detector signal from a μMUX channel. The noise level for an input power of ~ – 45 dBm is around – 95 dBc/Hz, and for an almost full-scale value, is well below – 120 dBc/Hz. With these results, the GFB channelizer becomes an interesting tool for multi-tonal signal channelization for the readout of cryogenic sensors utilizing a μMUX, as it does not degrade the system performance. It presents high configuration flexibility capabilities, spectral leakage control, adaptability (using different window functions and sizes), and noise levels in the order of other state-of-the-art approaches, like polyphase filter banks and multi-channel digital down converters.

Acknowledgements Luciano Pablo Ferreyro is supported by the Consejo Nacional de Investigaciones Científicas y Técnicas (CONICET) as well as for the Helmholtz International Research School in Astroparticles and Enabling Technologies (HIRSAP). Luciano Pablo Ferreyro also acknowledges the support of the Karlsruhe School of Elementary and Astroparticle Physics: Science and Technology (KSETA).

Author Contributions All authors reviewed the manuscript.

Funding Open Access funding enabled and organized by Projekt DEAL.

Declarations

Conflict of interest The authors declare no conflict of interest.

References

1. L. Gastaldo, K. Blaum, K. Chrysalidis, T.D. Goodacre, A. Domula, M. Door, H. Dorrer, C.E. Düllmann, K. Eberhardt, S. Eliseev, C. Enss, A. Faessler, P. Filianin, A. Fleischmann, D. Fonnesu, L. Gamer, R. Haas, C. Hassel, D. Hengstler, J. Jochum, K. Johnston, U. Kebschull, S. Kempf, T. Kieck, U. Köster, S. Lahiri, M. Maiti, F. Mantegazzini, B. Marsh, P. Neroutsos, Y.N. Novikov, P.C.O. Ranitzsch, S. Rothe, A. Rischka, A. Saenz, O. Sander, F. Schneider, S. Scholl, R.X. Schüssler, C. Schweiger, F. Simkovic, T. Stora, Z. Szücs, A. Türler, M. Veinhard, M. Weber, M. Wegner, K. Wendt, K. Zuber, The electron capture in ^{163}Ho experiment - ECHo. Eur. Phys. J. Spec. Top. **226**, 1623–1694 (2017). https://doi.org/10.1140/epjst/e2017-70071-y
2. A. Fleischmann, L. Gastaldo, S. Kempf, A. Kirsch, A. Pabinger, C. Pies, J.-P. Porst, P. Ranitzsch, S. Schäfer, F. Seggern, T. Wolf, C. Enss, G.M. Seidel, B. Young, B. Cabrera, A. Miller, Metallic magnetic calorimeters In: AIP Conference Proceedings (AIP Publishing, 2009), pp. 571–578. https://doi.org/10.1063/1.3292407
3. J.-C. Hamilton, L. Mousset, E.S. Battistelli, P. Bernardis, M.-A. Bigot-Sazy, P. Chanial, R. Charlassier, G. D'Alessandro, M.D. Petris, M.M.G. Lerena, L. Grandsire, S. Landau, S. Mandelli, S. Marnieros, S. Masi, A. Mennella, C. O'Sullivan, M. Piat, G. Ricciardi, C.G. Scóccola, M. Stolpovskiy, A. Tartari, S.A. Torchinsky, F. Voisin, M. Zannoni, P. Ade, J.G. Alberro, A. Almela, G. Amico, L.H. Arnaldi, D. Auguste, J. Aumont, S. Azzoni, S. Banfi, A. Baù, B. Bélier, D. Bennett, L. Bergé, J.-P. Bernard, M. Bersanelli, J. Bonaparte, J. Bonis, E. Bunn, D. Burke, D. Buzi, F. Cavaliere, C. Chapron, A.C.C. Cerutti, F. Columbro, A. Coppolecchia, G.D. Gasperis, M.D. Leo, S. Dheilly, C. Duca, L. Dumoulin, A. Etchegoyen, A. Fasciszewski, L.P. Ferreyro, D. Fracchia, C. Franceschet, K.M. Ganga, B. García, M.E.G. Redondo, M. Gaspard, D. Gayer, M. Gervasi, M. Giard, V. Gilles, Y. Giraud-Heraud, M.G. Berisso, M. González, M. Gradziel, M.R. Hampel, D. Harari, S. Henrot-Versillé, F. Incardona, E. Jules, J. Kaplan, C. Kristukat, L. Lamagna, S. Loucatos, T. Louis, B. Maffei, W. Marty, A. Mattei, A. May, M. McCulloch, L. Mele, D. Melo, L. Montier, L.M. Mundo, J.A. Murphy, J.D. Murphy, F. Nati, E. Olivieri, C. Oriol, A. Paiella, F. Pajot, A. Passerini, H. Pastoriza, A. Pelosi, C. Perbost, M. Perciballi, F. Pezzotta, F. Piacentini, L. Piccirillo, G. Pisano, M. Platino, G. Polenta, D. Prêle, R. Puddu, D. Rambaud, E. Rasztocky, P. Ringegni, G.E. Romero, J.M. Salum, A. Schillaci, S. Scully, S. Spinelli, G. Stankowiak, A.D. Supanitsky, J.-P. Thermeau, P. Timbie, M. Tomasi, C. Tucker, G. Tucker, D. Viganò, N. Vittorio, F. Wicek, M. Wright, A. Zullo, QUBIC I: overview and science program. J. Cosmol. Astropart. Phys. **2022**, 034 (2022). https://doi.org/10.1088/1475-7516/2022/04/034
4. A.H. Guth, Inflationary universe: a possible solution to the horizon and flatness problems. Phys. Rev. D **23**, 347–356 (1981). https://doi.org/10.1103/PhysRevD.23.347
5. A.D. Linde, A new inflationary universe scenario: a possible solution of the horizon, flatness, homogeneity, isotropy and primordial monopole problems. Phys. Lett. B **108**(6), 389–393 (1982). https://doi.org/10.1016/0370-2693(82)91219-9

6. S. Marnieros, P. Ade, J.G. Alberro, A. Almela, G. Amico, L.H. Arnaldi, D. Auguste, J. Aumont, S. Azzoni, S. Banfi, P. Battaglia, E.S. Battistelli, A. Baù, B. Bélier, D. Bennett, L. Bergé, J.-P. Bernard, M. Bersanelli, M.-A. Bigot-Sazy, N. Bleurvacq, J. Bonaparte, J. Bonis, A. Bottani, E. Bunn, D. Burke, D. Buzi, F. Cavaliere, P. Chanial, C. Chapron, R. Charlassier, F. Columbro, A. Coppolecchia, G. D'Alessandro, P. Bernardis, G.D. Gasperis, M.D. Leo, M.D. Petris, S. Dheilly, L. Dumoulin, A. Etchegoyen, A. Fasciszewski, L.P. Ferreyro, D. Fracchia, C. Franceschet, M.M.G. Lerena, K. Ganga, B. García, M.E.G. Redondo, M. Gaspard, D. Gayer, M. Gervasi, M. Giard, V. Gilles, Y. Giraud-Heraud, M.G. Berisso, M. González, M. Gradziel, L. Grandsire, J.-C. Hamilton, D. Harari, S. Henrot-Versillé, D.T. Hoang, F. Incardona, E. Jules, J. Kaplan, C. Kristukat, L. Lamagna, S. Loucatos, T. Louis, B. Maffei, W. Marty, S. Masi, A. Mattei, A. May, M. McCulloch, L. Mele, S. Melhuish, A. Mennella, L. Montier, L. Mousset, L.M. Mundo, J.A. Murphy, J.D. Murphy, F. Nati, E. Olivieri, C. Oriol, C. O'Sullivan, A. Paiella, F. Pajot, A. Passerini, H. Pastoriza, A. Pelosi, C. Perbost, M. Perciballi, F. Pezzotta, F. Piacentini, M. Piat, L. Piccirillo, G. Pisano, M. Platino, G. Polenta, D. Prêle, R. Puddu, D. Rambaud, P. Ringegni, G.E. Romero, M. Salatino, J.M. Salum, A. Schillaci, C. Scóccola, S. Scully, S. Spinelli, G. Stankowiak, M. Stolpovskiy, A. Tartari, J.-P. Thermeau, P. Timbie, M. Tomasi, S. Torchinsky, G. Tucker, C. Tucker, D. Viganò, N. Vittorio, F. Voisin, F. Wicek, M. Zannoni, A. Zullo, TES bolometer arrays for the QUBIC B-Mode CMB experiment. J. Low Temp. Phys. **199**(3–4), 955–961 (2020). https://doi.org/10.1007/s10909-019-02304-5
7. J.M. Geria, M.R. Hampel, S. Kempf, J.J.F. Bonaparte, L.P. Ferreyro, M.E.G. Redondo, D.A. Almela, J.M.S. Salum, N.A. Müller, J.D.B. Neira, A.E. Fuster, M. Platino, A. Etchegoyen, Suitability of magnetic microbolometers based on paramagnetic temperature sensors for CMB polarization measurements. J. Astron. Telesc. Instrum. Syst. (2023). https://doi.org/10.1117/1.jatis.9.1.016002
8. M. Wegner, N. Karcher, O. Krömer, D. Richter, F. Ahrens, O. Sander, S. Kempf, M. Weber, C. Enss, Microwave SQUID multiplexing of metallic magnetic calorimeters: status of multiplexer performance and room-temperature readout electronics development. J. Low Temp. Phys. **193**(3–4), 462–475 (2018). https://doi.org/10.1007/s10909-018-1878-3
9. L.P. Ferreyro, M.G. Redondo, M.R. Hampel, A. Almela, A. Fuster, J. Salum, J.M. Geria, J. Bonaparte, J. Bonilla-Neira, N. Müller, N. Karcher, O. Sander, M. Platino, M. Weber, A. Etchegoyen, An implementation of a channelizer based on a Goertzel Filter Bank for the read-out of cryogenic sensors. J. Instrum. **18**(06), 06009 (2023). https://doi.org/10.1088/1748-0221/18/06/p06009
10. AMD Xilinx: UG1137 - Zynq UltraScale+ MPSoC Software Developer Guide. (2023). https://docs.xilinx.com/r/en-US/ug1137-zynq-ultrascale-mpsoc-swdev
11. Analog Devices: AD-FMCDAQ2-EBZ. https://www.analog.com/en/design-center/evaluation-hardware-and-software/evaluation-boards-kits/eval-ad-fmcdaq2-ebz.html
12. R. Gartmann, N. Karcher, R. Gebauer, O. Krömer, O. Sander, Progress of the ECHo SDR readout hardware for multiplexed MMCs. J. Low Temp. Phys. **209**(3–4), 726–733 (2022). https://doi.org/10.1007/s10909-022-02854-1
13. Bluefors: Dilution Refrigerator Measurement Systems - LD250. https://bluefors.com/products/dilution-refrigerator-measurement-systems/
14. Low Noise Factory: LNF - LNC 4-8 GHz Ultra Low Noise Amplifier. https://lownoisefactory.com/product/lnf-lnc4_8f/
15. B. Dober, Z. Ahmed, K. Arnold, D.T. Becker, D.A. Bennett, J.A. Connors, A. Cukierman, J.M. D'Ewart, S.M. Duff, J.E. Dusatko, J.C. Frisch, J.D. Gard, S.W. Henderson, R. Herbst, G.C. Hilton, J. Hubmayr, Y. Li, J.A.B. Mates, H. McCarrick, C.D. Reintsema, M. Silva-Feaver, L. Ruckman, J.N. Ullom, L.R. Vale, D.D.V. Winkle, J. Vasquez, Y. Wang, E. Young, C. Yu, K. Zheng, A microwave SQUID multiplexer optimized for bolometric applications. Appl. Phys. Lett. (2021). https://doi.org/10.1063/5.0033416
16. Picotest: G5100A Waveform Generator. https://www.picotest.com/products_G5100A.html
17. J.A.B. Mates, G.C. Hilton, K.D. Irwin, L.R. Vale, K.W. Lehnert, Demonstration of a multiplexer of dissipationless superconducting quantum interference devices. Appl. Phys. Lett. (2008). https://doi.org/10.1063/1.2803852
18. J.M. Salum, T. Muscheid, A. Fuster, M.E.G. Redondo, M.R. Hampel, L.P. Ferreyro, J.M. Geria, J. Bonilla-Neira, N. Müller, J. Bonaparte, A. Almela, L.E. Ardila-Perez, M. Platino, O. Sander, M. Weber, Aliasing effect on flux ramp demodulation: nonlinearity in the microwave squid multiplexer. J. Low Temp. Phys. **213**(3–4), 223–236 (2023). https://doi.org/10.1007/s10909-023-02993-z